



Comparison of pressure-saturation characteristics derived from computed tomography and lattice Boltzmann simulations

Marcel G. Schaap,¹ Mark L. Porter,² Britt S. B. Christensen,³ and Dorthe Wildenschild²

Received 10 November 2006; revised 18 September 2007; accepted 10 October 2007; published 7 December 2007.

[1] A Shan-Chen-type multiphase lattice Boltzmann (LB) model was applied to observed computed microtomography data from water-air and water-Soltrol displacement experiments in a glass bead porous medium. Analysis of the Bond, Reynolds, and Capillary numbers for these systems showed that capillary forces were dominant removing the need to model viscous, gravitational, and density effects. A numerical parameterization of the LB model yielded lattice surface tension and contact angle, and appropriate pressure boundary conditions. Two scaling relations provided a link between lattice pressure and physical pressure and lattice time and physical time. Results showed that there was a good match between measured and simulated pressure-saturation data for the water-air system, but that there were large differences between the simulations and observations for the water-Soltrol system. The discrepancies for the water-Soltrol system were probably due to inconsistencies between experimental conditions and simulated conditions such as nonzero contact angle in the experiments. Analysis of saturation profiles indicated increasing saturation near the wetting boundary and decreasing saturations near the nonwetting boundary. We attribute these saturation transitions to pore-neck and percolation effects. While computationally intensive, results of this study were very encouraging for the application of LB simulations to microscale interfacial phenomena. Future studies will carry out a further validation in terms of interfacial areas, contact lines, and fluid distributions.

Citation: Schaap, M. G., M. L. Porter, B. S. B. Christensen, and D. Wildenschild (2007), Comparison of pressure-saturation characteristics derived from computed tomography and lattice Boltzmann simulations, *Water Resour. Res.*, 43, W12S06, doi:10.1029/2006WR005730.

1. Introduction

[2] Lattice Boltzmann (LB) methods have become increasingly popular for simulating fluid dynamics in a wide variety of applications including multiphase flow in porous media [e.g., *Chen and Doolen*, 1998; *Succi*, 2001; *Nourgaliev et al.*, 2003]. In contrast to methods like pore network models [e.g., *Vogel*, 2000; *Nordhaug et al.*, 2003] the LB method does not need an intermediate step to transform the observed pore space into a pore network. A clear advantage of the LB method over finite difference methods [e.g., *Adler et al.*, 1990; *Masad et al.*, 2000] is its relative simplicity and its ability to deal with arbitrary geometries. In addition, LB methods can be coded very efficiently and run on parallel computers or computer clusters, reducing cost and computation time.

[3] Several approaches are available to implement multiphase fluid behavior in LB models. The oldest model is that by *Rothman and Keller* [1988] (R-K) and was subsequently

modified by *Gunstensen and Rothman* [1991] and *Tölke et al.* [2002]. In this model the collision operator (explained later) is split in three parts [*Tölke et al.*, 2002], such that fluid separation may be obtained. A free parameter is used to control the surface tension. *Shan and Chen* [1993, 1994] (S-C) and *Martys and Chen* [1996] developed models that implemented liquid-vapor phase separation according to a nonideal equation of state and immiscible fluid-fluid separation induced by a repulsive interaction. Surface tension and solid phase wettability and contact angle are controlled by two parameters [*Martys and Chen*, 1996]. *Swift et al.* [1995, 1996] and *Angelopoulos et al.* [1998] proposed a model based on a thermodynamically consistent definition of vapor and liquid densities, surface tension, interface thickness, chemical potential, viscosity, and temperature. *Inamuro et al.* [2004a, 2004b] extended this model for incompressible two-phase flows with large density differences. Potential problems with the *Swift et al.* [1995, 1996] LB model and variants are their computational complexity and the fact that their thermodynamic basis has been questioned [*Házi et al.*, 2002; *Nourgaliev et al.*, 2003].

[4] Lattice Boltzmann simulations have successfully been applied to saturated porous media [e.g., *Ferréol and Rothman*, 1995; *Heijs and Lowe*, 1995; *Pan et al.*, 2001; *Zhang et al.*, 2000, 2002a, 2002b, 2005]. There is also an increasingly large body of work on multiphase LB simulations in porous media [e.g., *Angelopoulos et al.*, 1998; *Házi et al.*, 2002; *Sukop and Or*, 2004; *Pan et al.*, 2004a; *Chau et al.*, 2005;

¹Department of Soil, Water and Environmental Science, University of Arizona, Tucson, Arizona, USA.

²Department of Chemical, Biological, and Environmental Engineering, Oregon State University, Corvallis, Oregon, USA.

³Department of Hydrology, Geological Survey of Denmark and Greenland (GEUS), Copenhagen, Denmark.

Vogel et al., 2005]. However, despite recent advances, comparison of multiphase LB results with microscopic observations still is a somewhat unexplored terrain. *Pan et al.* [2004a] compared LB simulations at different resolutions with an observed macroscale water-NAPL pressure saturation curve obtained by *Hilpert et al.* [2001]. Although the porous geometry was not observed, but generated by a particle packing algorithm [*Hilpert and Miller*, 2001], a good correspondence between observed and simulated pressure saturation data was obtained for all but the coarsest resolutions. *Vogel et al.* [2005] used representations of an observed 3-D sintered glass bead pore geometry to simulate pressure saturation characteristics using a full morphology model [*Hazlett*, 1995; *Hilpert and Miller*, 2001], a pore network model [*Vogel*, 2000] and a lattice Boltzmann model [*Tölke et al.*, 2002] and found a high degree of correspondence among the models. However, owing to practical difficulties, a comparison with experimental data was not made.

[5] Parallel to the development of LB and other numerical methods applicable to the pore scale, great advances have also been made in the pore-scale observations of solid and fluid interfacial geometries. Computed microtomography (CMT) using high-brilliance synchrotron X-ray radiation has been especially useful in gaining quantitative insight of pore-scale and interfacial phenomena [e.g., *Hazlett*, 1995; *Ferréol and Rothman*, 1995; *Coles et al.*, 1998; *Wildenschild et al.*, 2002, 2005; *Prodanović et al.*, 2006]. Two sets of rigorously designed and CMT-observed flow experiments were reported by *Culligan et al.* [2004, 2006]. In both experiments, a glass-bead porous medium was subjected to several imbibition-drainage cycles for water-air [*Culligan et al.*, 2004] and water-Soltrol 220 [*Culligan et al.*, 2006]. CMT scanning was performed and capillary pressures and saturations were determined at several points on each drainage-imbibition cycle. Quantitative image analysis on the CMT data was applied to delineate fluid and interfacial distributions, saturations, and interfacial areas (further experimental details follow).

[6] The objective of this paper is to apply LB modeling to an observed microscale multiphase pore geometry obtained by *Culligan et al.* [2004, 2006] and to compare observed and simulated pressure-saturation characteristics. We selected a Shan-Chen-type two-component model by *Martys and Chen* [1996] over other models because of its conceptual and computational simplicity and because it was successfully used in previous work [*Raiskinmäki et al.*, 2001; *Pan et al.*, 2004a; *Sukop and Or*, 2004; *Chau et al.*, 2005].

[7] In the following we will first summarize the relevant experimental data reported by *Culligan et al.* [2004, 2006]. Subsequently, we will describe the basic single component LB model and the two-component extension by *Martys and Chen* [1996]. Next, we will investigate how to represent the experimental conditions in simplified form and deal with conversion of lattice-scale pressure and time to “physical” pressure and time. By calibrating fluid cohesion and fluid-solid adhesion parameters in the S-C model we will subsequently set surface tension and a zero contact angle and obtain the appropriate pressure boundary conditions. Further implementation details for reduction of CPU time and representing the experimental system are discussed next. Finally, we will present simulation results for imbibition and

drainage in terms of equilibration times, saturation profiles, and compare simulated pressure saturation characteristics of the water-air and the water-Soltrol systems with observed data.

2. Materials and Methods

2.1. Experimental System

[8] Here we summarize the procedures that were followed to acquire pressure-saturation data for water-air and water-Soltrol-220 displacement experiments; details are given by *Culligan et al.* [2004, 2006] and *Wildenschild et al.* [2005]. Both experiments were carried out at the Geo-SoilEnviro Consortium for Advanced Radiation Sources (GSECARS) bending magnet beamline, Advanced Photon Source, Argonne National Laboratory.

[9] The displacement experiments were carried out in a 70 mm tall and 7 mm inner diameter acrylic column filled with soda lime glass beads with sizes between 0.6 to 1.4 mm (Figure 1). The bottom of the column was connected to a pressure transducer and a syringe pump (Harvard Apparatus, Inc., model 44) through a water wet 1.2 μm semipermeable membrane. The pressure transducer measured the capillary pressure, while the syringe pump was used to pump a precise amount of water into or out of the sample at predetermined rates [*Culligan et al.*, 2004, 2006]. The top of the sample was connected to the open air (with measures to prevent evaporation) or a Soltrol 220 reservoir.

[10] For the water-air system a primary drainage characteristic was measured starting from a water saturated sample using a Darcy flow velocity of $1.8 \cdot 10^{-6}$ m/s. Subsequent imbibition and drainage cycles took place at the same flow velocity, whereas the next imbibition-drainage cycle was conducted at a flow velocity of $1.4 \cdot 10^{-6}$ m/s. In the case of the water-Soltrol system the sequence started with a primary imbibition curve at $3.6 \cdot 10^{-6}$ m/s, followed by a primary drainage curve at the same flow velocity. Two secondary imbibition-drainage cycles were run at $3.6 \cdot 10^{-6}$ m/s and $2.2 \cdot 10^{-5}$ m/s, respectively. The displacements were applied briefly followed by 10 min of equilibration time and 10 min of tomographic imaging, allowing a pressure saturation point to be obtained every 30 min. The resulting capillary pressures for the air water system were between 0 and 1100 Pa (73 points) and predominantly between 0 and 350 Pa (48 points) for the water-Soltrol system. From additional laboratory experiments it was concluded that the pressure saturation characteristics were in near-equilibrium [*Culligan et al.*, 2006].

[11] Computed microtomography (CMT) using monochromatic X-ray radiation was used to image the three-dimensional distribution of solid, wetting, and nonwetting phases at a resolution of 17 μm per voxel. In order to create a significant wetting/nonwetting/solid contrast at 33.3 keV X-ray energy it was necessary to use a 0.1 M KI solution as the wetting phase, thus increasing the density of water to 1140 kg/m^3 ; no dopant was used in the Soltrol. Because of experimental and computational constraints it was only possible to image the middle 5 mm of the column, however, *Culligan et al.* [2004] showed that a representative elementary volume was contained in this section. Image analysis on the acquired data was performed to reduce noise, identify solid wetting and nonwetting phases, determine fluid satu-

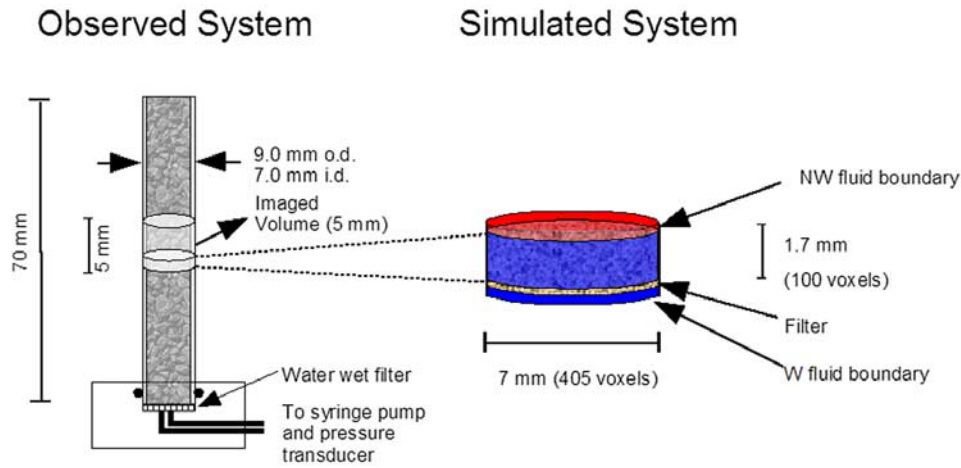


Figure 1. Schematic overview of the experimental setup (left), the CMT imaged part and the representation of the experimental system in the lattice Boltzmann simulations (right, not to scale).

rations, and interfacial areas [Culligan *et al.*, 2004, 2006; Wildenschild *et al.*, 2002, 2005].

[12] Table 1 contains the most pertinent experimental data for the water-air and water-Soltrol experiments. We note that different values for the surface tension of Soltrol 220 have been reported in the literature with a range between 0.030 and 0.048 N/m with some uncertainties about the exact experimental conditions [Bradford and Leij, 1996;

Kechavarzi *et al.*, 2000, 2005; Liu *et al.*, 1998; Schroth *et al.*, 1995]. In this paper we will be using a value of 0.0378 N/m (M. Tuller, University of Arizona, Tucson, personal communication, 2007). We assumed a water-wet solid phase and a zero contact angle in both the water-air and water-Soltrol systems. The characteristic pore radius, R_{char} , was 1.031×10^{-4} m and derived from the pore volume and the specific surface area of the solid phase using

Table 1. Properties of the Experimental Systems^a

Property	Value	Units
Porosity, ϕ	0.34	
Resolution (voxel size), h_p	1.7×10^{-5}	m
Sample height (imaged section), H_s	6.1×10^{-3} (360)	m (voxels)
Sample diameter, D_s	6.9×10^{-3} (405)	m (voxels)
Average cross-sectional pore area, A	1.262×10^{-5}	m ²
Average cross-sectional solid surface perimeter, C	0.247	m
Characteristic pore radius, $R_{char} = 2A/C$	1.031×10^{-4}	m
Gravitational acceleration, g	9.81	m/s ²
<i>Water-Air System</i>		
Water density, 0.1M KI solution, ρ_w (20°C)	1.140×10^3	kg/m ³
Air density, ρ_a	1.25	kg/m ³
Water-air surface tension, σ_{wa} (20°C)	0.7275	N/m
Water dynamic viscosity, μ_w (20°C)	1.002×10^{-3}	Pa s
Air dynamic viscosity, μ_a (25°C)	18.6×10^{-6}	Pa s
Darcy flow velocity range, u_w	1.8×10^{-6} to 1.4×10^{-5}	m/s
Capillary pressure range, P_c	0 to 1100	Pa
Water saturation range, S_w	0.04 to 1.0	
Bond number, $Bo = \frac{g(\rho_w - \rho_a)R_{char}^2}{\sigma_{wa}}$	1.63×10^{-3}	
Capillary number, $Ca = \frac{u_w \mu_w}{\sigma_{wa}}$	2.47×10^{-8} to 1.92×10^{-7}	
Reynolds number, $Re = \frac{\rho_w u_w R_{char}}{\mu_w}$	2.12×10^{-4} to 1.65×10^{-3}	
<i>Water-Soltrol-220 System</i>		
Soltrol density, ρ_s (23°C)	0.79×10^3	kg/m ³
Water Soltrol-220 interfacial tension, σ_{ws} (see text)	0.0378	N/m
Soltrol dynamic viscosity, μ_o (23°C)	4.82×10^{-3}	Pa s
Darcy flow velocity range, u_w	3.6×10^{-6} to 2.2×10^{-5}	m/s
Capillary pressure range, P_c	0 to 300	Pa
Water saturation range, S_w	0.131 to 0.892	
Bond number, $Bo = \frac{g(\rho_w - \rho_s)R_{char}^2}{\sigma_{ws}}$	9.65×10^{-4}	
Capillary number, $Ca = \frac{u_w \mu_s}{\sigma_{ws}}$	4.59×10^{-7} to 2.81×10^{-6}	
Reynolds number, $Re = \frac{\rho_s u_w R_{char}}{\mu_s}$	6.08×10^{-5} to 3.72×10^{-4}	

^aSee text for more information.

Table 2. Coordinate System and Link Classification for the D3Q19 Model Used in This Study^a

Link	0	1	2	3	4	5	6	7	8	9	10	11	12	13	14	15	16	17	18
Type	I	II	III	II															
x	0	1	1	0	-1	-1	-1	0	1	0	1	0	-1	0	1	0	-1	0	0
y	0	0	1	1	1	0	-1	-1	-1	0	0	1	0	-1	0	1	0	-1	0
z	0	0	0	0	0	0	0	0	0	1	1	1	1	1	-1	-1	-1	-1	-1

^aThe vector \mathbf{e}_i is derived from the x , y , and z rows for each link.

two-point correlation function analysis [Blair *et al.*, 1996; Schaap and Lebron, 2001].

2.2. Lattice Boltzmann Model

2.2.1. Single Component Model

[13] Lattice Boltzmann methods are fluid dynamics models that compute the evolution of particle distributions in highly discretized space and time. The D3Q19 model [Qian *et al.*, 1992; Martys and Chen, 1996] implements a three-dimensional model consisting of a regular lattice of nodes. Each node maintains a particle distribution, $f_i(\mathbf{x}, t)$, where the subscript i is the index of the 19 members, 18 of which form links that point to neighboring nodes with relative positions indicated by the vectors \mathbf{e}_i (Table 2); \mathbf{x} is the discrete location of each node (x, y, z coordinates), and t is the discrete time. There are three types of links: a single type I link in the center that does not point to neighboring nodes, six Type II links that point to the nearest neighbor nodes, and 12 type III links that point to the next nearest neighbors (Table 2). The corresponding speeds are 0, 1 and $\sqrt{2}$, respectively, with lattice spacing $\Delta x = 1$ and time step $\Delta t = 1$.

[14] To evolve a lattice Boltzmann system in time and space, three operations are applied for every time step. In step 1, the macroscopic quantities number density (mass), $n(\mathbf{x}, t)$, pressure, $P(\mathbf{x}, t)$, and the velocity vector, $\mathbf{u}(\mathbf{x}, t)$, are computed from $f_i(\mathbf{x}, t)$ with

$$n(\mathbf{x}, t) = \sum_{i=0}^{18} f_i(\mathbf{x}, t), \quad (1)$$

$$P(\mathbf{x}, t) = \frac{n(\mathbf{x}, t)}{3}, \quad (2)$$

$$\mathbf{u}(\mathbf{x}, t) = \frac{1}{n(\mathbf{x}, t)} \sum_{i=0}^{18} f_i(\mathbf{x}, t) \mathbf{e}_i. \quad (3)$$

In step 2, $n(\mathbf{x}, t)$, and $\mathbf{u}(\mathbf{x}, t)$ are used to compute the equilibrium distribution, $f_i^{eq}(\mathbf{x}, t)$. The equilibrium distribution defines the particle distribution that should be present at a node given $n(\mathbf{x}, t)$ and $\mathbf{u}(\mathbf{x}, t)$; it is parameterized such that mass and momentum are conserved [Qian *et al.*, 1992; Martys and Chen, 1996],

$$f_0^{eq}(\mathbf{x}, t) = \omega_0 n(\mathbf{x}, t) \left(1 - \frac{3}{2} \mathbf{u}(\mathbf{x}, t)^2 \right) \quad (4a)$$

$$f_i^{eq}(\mathbf{x}, t) = \omega_i n(\mathbf{x}, t) \left(1 + 3\mathbf{e}_i \cdot \mathbf{u}(\mathbf{x}, t) + \frac{3}{2} \left[3(\mathbf{e}_i \cdot \mathbf{u}(\mathbf{x}, t))^2 - \mathbf{u}(\mathbf{x}, t)^2 \right] \right), \quad (4b)$$

where $\omega_0 = 1/3$, $\omega_i = 1/18$ for links of type II, and $\omega_i = 1/36$ for links of type III. In step 3, the collision step, $f_i(\mathbf{x}, t)$ is partially or entirely replaced with the equilibrium distribution depending on the value of a relaxation parameter, τ . Subsequently, a streaming operator (the actual time step) ensures that particle distribution members of each distribution replace the corresponding particle distribution members in surrounding nodes. The streaming and collision operators are commonly combined as

$$f_i(\mathbf{x} + \mathbf{e}_i, t + 1) = f_i(\mathbf{x}, t) - \frac{1}{\tau} [f_i(\mathbf{x}, t) - f_i^{eq}(n(\mathbf{x}, t), \mathbf{u}(\mathbf{x}, t))]. \quad (5)$$

Thus link 1 present at location (x, y, z) at time t will replace link 1 present in the distribution at $(x + 1, y, z)$ at time $t + 1$, while link 2 will replace link 2 at $(x + 1, y + 1, z)$ etcetera (see Table 2). Links that point into a solid phase node are treated with the ‘‘bounce-back’’ rule [e.g., Chen and Doolen, 1998, and references therein]. Simply put, the mass that would go into the neighboring solid node is assigned to the opposing link, thus conserving mass and momentum. In this scheme, the mass of link 1 of node (x, y, z) is assigned to link 5 of node (x, y, z) if there is a solid node at $(x + 1, y, z)$. Improved schemes are available [e.g., Pan *et al.*, 2006] but these were not used in the present study to conserve CPU time.

[15] The relaxation parameter, τ , determines how quickly the system evolves to equilibrium; τ is related to a lattice kinematic viscosity, ν_L , as [Qian *et al.*, 1992]

$$\nu_L = \frac{c^2[\tau - 0.5]}{6}, \quad (6)$$

where c is the lattice constant [Martys and Douglas, 2001].

2.2.2. Multiple Component Extensions

[16] Shan and Chen [1993, 1994] and Martys and Chen [1996] extended the single component LB model to account for miscible and immiscible fluid systems by using two distribution functions, resulting in the presence of two components with number densities n_1 and n_2 at each node. Interaction between the components allows for fluid separation with one of the components dominating in each phase (major component) and the other being present as a minor component. Fluid separation will usually lead to curved fluid interfaces and the notion of surface tension. By having component interaction with the solid phase it is also possible to set wettability and a fluid-solid contact angle. To facilitate notation, we will index n_1 and n_2 with α .

[17] Fluid-fluid, fluid-solid interactions, and gravitational effects are implemented in the S-C model by modifying the momentum of the components (dependence on t dropped for clarity),

$$n_\alpha(\mathbf{x}) \mathbf{u}'(\mathbf{x}) = n_\alpha(\mathbf{x}) \mathbf{u}(\mathbf{x}) + \tau_\alpha [\mathbf{F}_{g,\alpha}(\mathbf{x}) + \mathbf{F}_{c,\alpha}(\mathbf{x}) + \mathbf{F}_{a,\alpha}(\mathbf{x})], \quad (7)$$

where $\mathbf{u}'(\mathbf{x})$ is the modified velocity, τ_α is the relaxation parameter of component α , and \mathbf{F}_g , \mathbf{F}_c , and \mathbf{F}_a are the gravitational, cohesion (interaction between fluid components), and adhesion forces (component to solid adhesion), respectively. Note that the velocity vector $\mathbf{u}(\mathbf{x})$ is not subscripted by α because we are effectively dealing with the mixture of two components, even if there is fluid separation. The effective ensemble velocity of the mixture is therefore [Martyis and Chen, 1996]

$$\mathbf{u}(\mathbf{x}) = \frac{\sum_{\alpha=1}^2 n_\alpha(\mathbf{x})\mathbf{u}_\alpha(\mathbf{x})/\tau_\alpha}{\sum_{\alpha=1}^2 n_\alpha(\mathbf{x})/\tau_\alpha}. \quad (8)$$

The ensemble mass is simply the sum over the component number densities present at each node. Fluid cohesion is calculated according to

$$\mathbf{F}_{c,\alpha}(\mathbf{x}) = -n_\alpha(\mathbf{x}) \sum_i^{18} G_{c,\alpha,\alpha',i} n_{\alpha'}(\mathbf{x} + \mathbf{e}_i) \mathbf{e}_i, \alpha \neq \alpha'. \quad (9)$$

The variables α and α' denote two different fluid components (i.e., 1 and 2 or 2 and 1, but not 1 and 1 or 2 and 2); in the S-C two-component model there is no interaction between components of the same type, nor interaction between the different components at the same node. Fluid miscibility is set by the interaction strength parameter $G_{c,\alpha,\alpha',i}$ which is equal to $2G_c$ for type II links, but equal to G_c for the longer type III links [Martyis and Chen, 1996]. The value of G_c should be positive and identical for both fluid components. Increasing G_c beyond a critical value will lead to progressively purer component mixtures. Pressure is now determined by both fluids and their interaction [Shan and Doolen, 1996],

$$P(\mathbf{x}) = \frac{n_1(\mathbf{x}) + n_2(\mathbf{x})}{3} + 12G_c n_1(\mathbf{x}) n_2(\mathbf{x}). \quad (10)$$

[18] Adhesive forces between solid phase and a fluid component are determined by the presence of solids in neighboring nodes that surround a fluid node,

$$F_{\alpha,a}(\mathbf{x}) = -n_\alpha(\mathbf{x}) \sum_i^{18} G_{\alpha,a,i} s(\mathbf{x} + \mathbf{e}_i) \mathbf{e}_i. \quad (11)$$

Here $s(\mathbf{x} + \mathbf{e}_i)$ is an indicator function that is set to 1 for a solid node and to 0 for a pore node. Similar to the fluid cohesion parameter, G_a controls the interaction strength and wetting properties of the fluids and $G_{a,a}$ is set to $2G_a$ for type II links and equal to G_a for type III links. A positive (negative) value is used for nonwetting (wetting) fluid and by changing the interaction strength a range of fluid-solid contact angles can be obtained. In this study we used a positive value for n_1 (nonwetting fluid, NW) and a negative value for n_2 (wetting fluid, W), with $G_{a,1} = -G_{a,2}$.

3. System Simplification, Calibration, and Implementation

3.1. System Simplification

[19] The two experimental systems each consist of two different fluids with contrasting densities and viscosities

which may complicate LB modeling (Table 1). While viscosity and density ratios of the water-Soltrol system can be implemented in the current S-C model, density ratios ($\sim 1:800$) and viscosity ratios (1:15 in terms of kinematic viscosity) of the water-air system are currently beyond the capabilities of this model. Models capable of dealing with these conditions do exist. For example, *Inamuro et al.* [2004a, 2004b] proposed a modification to the thermodynamic model by *Swift et al.* [1996] that allows for density ratios of 1:1000. However, we decided against this model because of its numerical complexity and apparent large demands on CPU time. It is therefore important to determine whether the experimental system can be represented in the S-C model in a simplified form.

[20] By calculating the dimensionless Bond (Bo , the ratio of gravitational and interfacial forces), Capillary (Ca , the ratio of viscous and capillary forces), and Reynolds numbers (Re , the ratio of inertial and viscous forces) we can evaluate which force dominates our water-air and water-Soltrol systems (Table 1). On the basis of the magnitude of the Bond number we can conclude that capillary forces acting on the fluids are much larger than the gravitational forces (e.g., buoyancy caused by density differences). Similarly, the Capillary number shows that viscous forces are negligible compared to capillary forces allowing us to disregard viscosity contrasts. The Reynolds number shows that inertial forces are much smaller than viscous forces, again showing that density differences probably do not play an important role and that the flow is distinctly laminar. These dimensionless quantities indicate that capillary forces dominate the system as also found by *Culligan et al.* [2006]. According to this analysis we can make the simplifying assumption that gravitational, inertial, and viscous forces do not have to be accounted for in the LB simulations presented here, allowing the S-C model to be applied to both the water-Soltrol and water-air systems.

[21] The analysis above implies that we must assign values to the lattice fluid-fluid and fluid-solid parameters, G_c and G_a , to get a lattice surface tension and an appropriate contact angle. For simulations where we impose pressure boundary conditions, it is also necessary to set the wetting and nonwetting component densities at each boundary to achieve a prescribed capillary pressure. In the following we offer an empirical way to set or calibrate the required values. The parameter τ was set to 1 and the same density was used for both fluids when the capillary pressure was zero.

3.2. Pressure and Time Scaling

[22] When relating physical space to lattice space it is convenient to define Laplace's law in a reduced physical scale by dividing the physical capillary pressure with the physical surface tension. There is still a space dimension, which can be removed by defining the space scale of the physical interfacial radius R_p as $h_p \Delta x$, where R_p and h_p are in physical units [m] and $\Delta x = 1$ (lattice units). The same approach can be used for the lattice scale. By equating the lattice terms to the scaled physical terms we can define an equation that provides the physical capillary pressure,

$$P_{c,p} = \frac{\sigma_p P_{c,L}}{h_p \sigma_L} [\text{Pa}]. \quad (12)$$

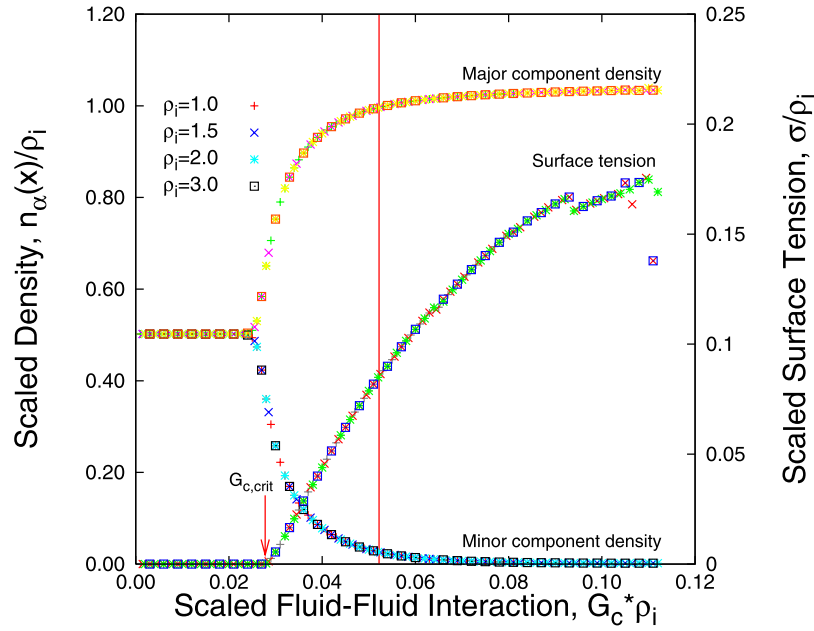


Figure 2. Scaled major and minor component densities in the bubble (left y axis) and scaled lattice surface tension (right y axis) as a function of the scaled cohesion parameter, $G_c \rho_i$. The simulations were carried out for four initial densities. The vertical line depicts the $G_c \rho_i$ value used in the rest of the study. $G_{c,crit}$ depicts the critical $G_c \rho_i$ value above which stable fluid separation is possible (see text).

In order to calculate the physical capillary pressure we need to know the resolution (h_p), the lattice capillary pressure, $P_{c,L}$, and the surface tension of the lattice and physical systems, α_L and σ_p , respectively. All these values are known from the experiments (Table 1) or can be derived from numerical experiments in the next section.

[23] Time scaling is obtained by relating the dynamic viscosity of water to the kinematic viscosity of the D3Q19 model,

$$\Delta t_p = \rho_w \nu_L \frac{h_p^2}{\mu_w} [\text{s}]. \quad (13)$$

For $\tau = 1$, we get a lattice kinematic viscosity, ν_L , of 0.1667 (equation (6)). By using the appropriate values of known quantities from Table 1, we obtain the physical time step $\Delta t_p = 5 \cdot 10^{-5}$ s per iteration. This means that about 20,000 iterations are needed to simulate 1 second of physical time in an air-water system, putting limitations on the physical size or physical time that can be simulated.

3.3. Lattice Density, Surface Tension, and Contact Angle

3.3.1. Density and Surface Tension

[24] In the S-C model there is a threshold value for G_c [Martys and Chen, 1996; Martys and Douglas, 2001] beyond which a uniformly mixed system of wetting and nonwetting components will yield a stable separation of two fluids,

$$G_c \geq \frac{1}{36(n_1 + n_2)}, \quad (14)$$

which gives a critical $G_{c,crit} = 0.02778$ for $n_2 + n_1 = 1$. To verify this we carried out four series of 2-D simulations

where we placed a pure bubble of nonwetting (NW) component (n_1) inside a 128×128 square of wetting (W) component (n_2) fluid with periodical boundaries; both fluids had equal total masses (i.e., the number of NW pixels was equal to the number of W pixels). Note that the naming of wetting and nonwetting fluid is still irrelevant in absence of a solid phase and is used here for continuity with later discussions. The four simulation series had initial densities of $\rho_i = 1.0, 1.5, 2.0$ and 3.0 (where $\rho_i = n_1 + n_2$) and the parameter G_c was increased in steps of 0.001 from zero until numerical instabilities occurred. Figure 2 shows the densities of the NW and W components inside the bubble, scaled with initial density. It is clear that for $0 \leq G_c \rho_i \leq 0.028$ the NW bubble dissolves into the W surrounding fluid, yielding scaled densities of 0.5 for each component. For $G_c \rho_i > 0.028$ the NW bubble becomes increasingly “pure,” with densities of NW eventually exceeding 1 for $G_c \rho_i > 0.054$ owing to the compressibility of the LB fluid. The density of the W component in the bubble rapidly drops to very low values with W:NW component ratios approaching $\approx 1:500$. Similar results, but with opposite component densities, are reached for the fluid outside the bubble.

[25] By determining the component densities inside and outside the bubble it is possible to calculate the lattice pressures of the wetting and nonwetting fluids (P_w and P_{nw}) using equation (10) and therefore the pressure difference across the interface (P_c). By determining the radius of the bubble, R , it is possible to compute the lattice surface tension by rearranging the two-dimensional version of Laplace’s law and accounting for the effect of initial density,

$$P_c = P_{nw} - P_w = \frac{\sigma_L}{\rho_i R}. \quad (15)$$

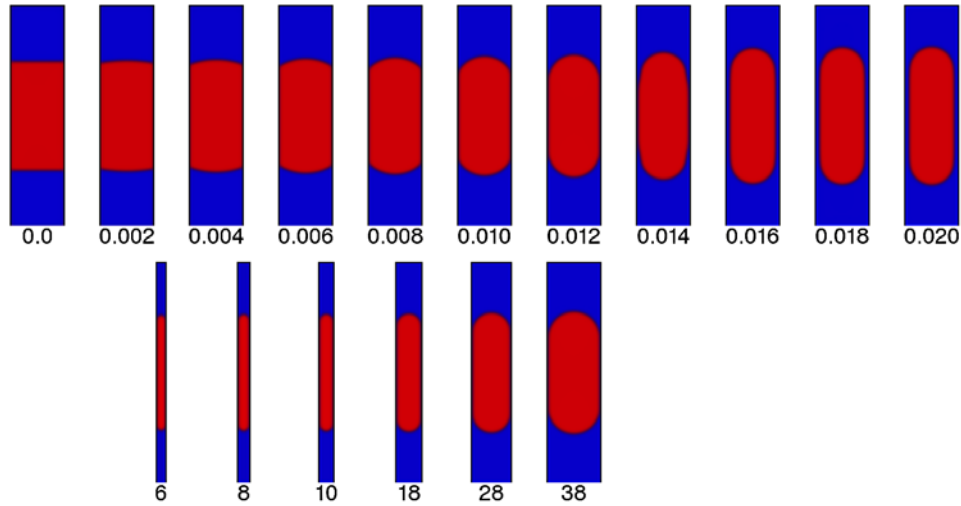


Figure 3. Tube simulations with enclosed wetting (blue) and nonwetting (red) fluids. The top row shows an increase in curvature for a nonwetting bubble in a duct with a wall to wall size of 38 pixels for $G_c \rho_i = 0.0522$ and G_a between 0 and 0.02. Bottom row shows results for $G_a = 0.012$ for ducts with wall to wall sizes between 6 and 38 voxels (not to scale with top row).

Figure 2 shows the dependence of σ_L on $G_c \rho_i$ (right hand axis), with values greater than zero for $G_c \rho_i > 0.028$. It appears that numerical instabilities occur beyond $G_c \rho_i = 0.09$.

[26] At this point we are free to choose a value for $G_c \rho_i$ between 0.028 and 0.09. On the one hand values close to 0.09 are preferable because this increases component contrasts within a fluid and reduces vapor-like diffusion and condensation effects, both of which do not play a major role in the experimental systems. On the other hand there are advantages to using a relatively low $G_c \rho_i$ value as this leads to a lower lattice surface tension and therefore an expanded physical pressure range (equation (12)). In practice, we found that $G_c \rho_i$ should be set to values smaller than 0.06 as otherwise numerical problems occurred when solid phase was present. Somewhat arbitrarily we set $G_c \rho_i$ to 0.0522, with an initial density, ρ_i , of 2.087. Using the data from the bubble simulations these values yield a σ_L / ρ_i value of 0.085 with typical component contrasts between 1:35 and 1:60, depending on the capillary pressure.

3.3.2. Contact Angle

[27] To set the contact angle and to check whether the presence of solid phase affects the surface tension, we enclosed equal masses of W fluid (blue) and a NW fluid (red) in a closed capillary consisting of a 3-D square duct [cf. *Martys and Chen, 1996, Figure 4*]. The NW fluid was placed in the middle of the capillary (Figure 3) with W on top and bottom; total masses of W and NW were equal. We set $G_c \rho_i$ to 0.0522 while G_a was varied between 0 and 0.02. The simulations were carried out for wall to wall duct sizes of 6, 8, 10, 18, 28 and 38 voxels with a duct length of 160 voxels. The simulations were run for 100,000 iterations at which point near-equilibrium was attained.

[28] The top row in Figure 3 shows that the contact angle changed from 90 degrees at $G_a = 0$ (neither fluid is wetting or nonwetting) to zero at $G_a = 0.012$ for ducts of size 38. The red nonwetting fluid detaches from the wall and an increasingly thicker film is formed for $G_a > 0.012$. However, no films were observed for the capillary pressure

conditions and image resolution of the micro tomography experiments. To prevent the simulation of excessive amounts of wetting phase films we therefore set G_a to 0.012. The bottom row in Figure 3 shows that $G_a = 0.012$ maintains a zero contact angle without films for a range of duct sizes.

[29] Figure 4 shows the dependence of contact angle and surface tension on G_a for the simulations shown in Figure 3. The surface tension was determined from the curvature of the interfaces, the pressure difference between the W and NW fluids, and Laplace's law (equation (15), with $2\sigma_L / [\rho_i R]$ for the 3-D case). The contact angle was found by calculating the angle of intersection of the fluid interface and the wall. There appears to be a slight dependence of the simulated contact angle on the duct sizes. The surface tension is constant for larger duct size, but some variation is visible for the smaller ducts. We note that curvature

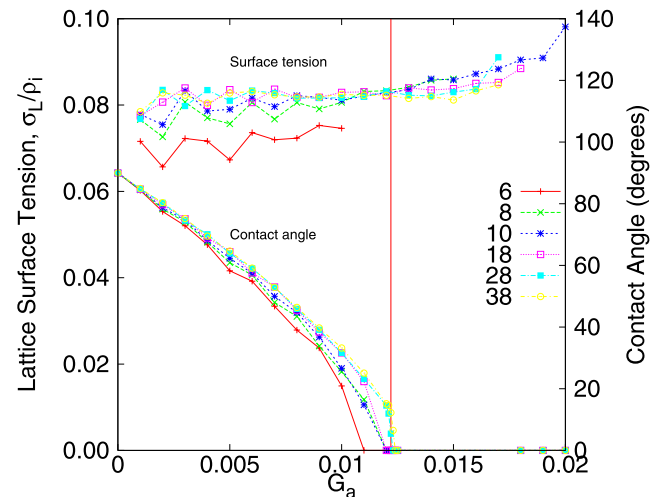


Figure 4. Surface tension and contact angle as a function of the value of the adhesion parameter, G_a , for several duct sizes. See also Figure 3.

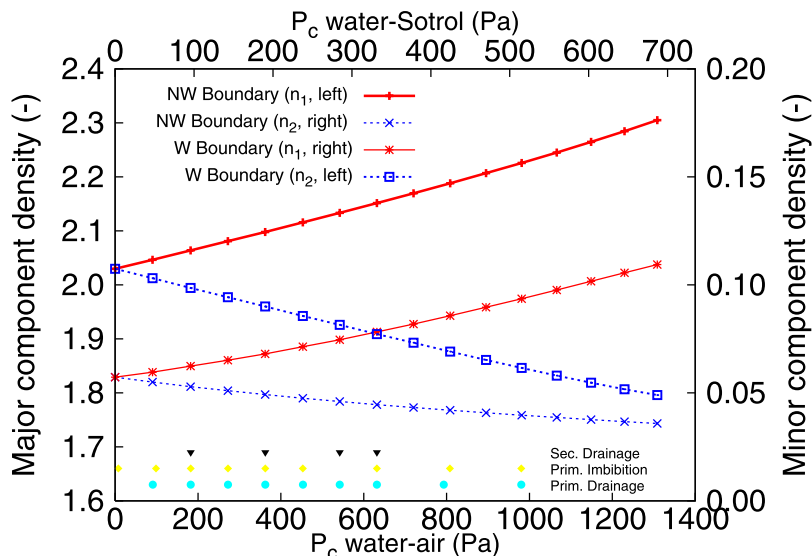


Figure 5. Component densities at the wetting and nonwetting boundaries with corresponding physical capillary pressures for the water-air and water-Solrol systems derived from the 3-D duct simulation with a wall to wall size of eight lattice units. Note that each fluid consists of a major and a minor component. The symbols at the bottom indicate for which pressure values simulations were carried out during primary and secondary drainage simulations and the primary imbibition simulation.

cannot be determined very precisely for small radii because of a limited number of pixels present in the interface. In addition, wall effects may play a relatively more important role for small radii as the effect of the fluid-solid interaction (equation (11)) causes a higher (lower) density of wetting (nonwetting) component near the wall. The corresponding σ_L/ρ_i value was 0.083, which is somewhat lower than that obtained from the 2-D bubble simulations (0.085), most likely because of wall effects.

3.3.3. Boundary Conditions

[30] The previous simulations were conducted for a system with periodic boundaries (the bubble simulations) or closed systems (the duct simulations). None of these simulations required external flux or pressure boundary conditions. However, in our representation of the experimental system it is necessary to impose pressures at the wetting and nonwetting ends of the simulated domain, thus yielding a capillary pressure inside the sample ($P_c = P_{nw} - P_w$). Both the wetting and the nonwetting pressures depend on the density of the two components, thus leading, in principle, to a system with four degrees of freedom from which to set the capillary pressure. At the same time it is important to keep the total mass in the system constant; otherwise a changing average density will change the value of $G_c\rho_i$ and therefore change the lattice surface tension (see Figure 2). The necessary data were obtained from the duct simulations.

[31] In the duct simulations the G_a parameter was varied such that we obtained a zero contact angle for $G_a = 0.012$ at which point the meniscus of the interface fitted exactly in the duct (see bottom row of Figure 3). For smaller values of G_a we obtained a meniscus with a larger radius and a nonzero contact angle. Given that the surface tension of these systems was approximately constant for $0 \leq G_a \leq 0.012$ (Figure 4), it is possible to use the wetting and nonwetting phase pressures and their corresponding com-

ponent densities to impose boundary conditions to our systems. In effect, the component densities inside the (non)-wetting fluid became our (non)wetting boundary densities. To impose the boundary conditions we chose the simulation with a duct size of 8 because, as shown in Figure 5, the range of capillary pressures associated with this system adequately covered what was needed for our physical systems. At $P_c = 0$ the major densities in the W and NW fluids are the same but at higher P_c the major component density in the NW fluid increases and that of the W fluid decreases; minor component densities show opposite trends. These results combined with equation (12) demonstrated that it is possible to conduct numerically stable LB simulations for capillary pressures between 0 and 680 Pa (water-Solrol) and 0 and 1300 Pa (water-air) for the systems outlined in Table 1; these are well within the range of the experimental conditions. However, using the data in Figure 5 and equation (10) it can be shown that there is also an 8.5% compressibility effect for a water-air P_c of 980 Pa making the NW fluid denser than the W fluid. Compressibility is almost linear with P_c and affects the volume of the two phases. It is also a relative effect, meaning that low wetting phase saturations of 0.1 at high P_c are overestimated by at most 1 or 2%. For the present study this error was sufficiently small to be neglected, but further study is warranted.

3.4. Implementation of the LB Pressure-Saturation Simulations

[32] Some compromises had to be made to represent the experimental systems in our LB simulations. The most important issue was that of the available CPU resources. The imaged system consists of approximately 59 million voxels ($405 \times 405 \times 360$ voxels), which required significant system RAM (approximately 12 gigabytes in single

precision) and very long computation times before a reasonable equilibrium was reached.

[33] Two options were available to reduce the CPU requirements. By doubling the node size, h_p , we can quadruple the simulated time step (equation (13)) and reduce the number of nodes by a factor of 8. At the same time, this will halve the maximum capillary pressure that can be simulated (equation (12)) thus limiting the pressure range over which LB simulations and experimental pressure-saturation curves can be compared.

[34] The other option was to simulate only part of the imaged volume. From *Culligan et al.* [2006] it follows that the average bead diameter was 0.86 mm and that a representative elementary volume REV for porosity and saturation was contained within a cube with a volume of 27 mm³ (REV sides of 3 mm). We decided to carry out the LB simulations at the original resolution of 17 microns and use only 100 layers of the 360 that were originally imaged (Figure 1). The resulting simulation domain represented a disc with a diameter of 7 mm and a height of 1.7 mm with a volume of 65 mm³, i.e., a volume over twice as large as what *Culligan et al.* [2006] found necessary for an REV. A disc shape was chosen rather than a cube because the disc included the walls of the experimental column, thus allowing us to use the standard “bounce back” algorithm to deal with the lateral boundaries. An additional reduction in CPU time was obtained by using the solid geometry of the water-Soltrol system also for the LB simulations of the water-air system. The same distribution of bead sizes was used for both experiments [*Culligan et al.*, 2004, 2006] with the only difference being that the beads of the water-Soltrol system were lightly sintered at high temperature to prevent movement during the experiment. Our assumption was that no statistical differences exist between the solid geometry of the water-Soltrol and water-air systems and that by using the appropriate physical surface tension and the assumption of a zero contact angle, equation (12) should yield the appropriate capillary pressures for both systems.

[35] Boundary conditions (Figure 5) were imposed to the top of the disc through a buffer of eight layers that were completely filled with nonwetting fluid (Figure 1). At the bottom we put a water wet filter [cf. *Pan et al.*, 2004a] and eight more layers for the wetting boundary. Although the experimental system was subject to intermittent flux boundary conditions [*Culligan et al.*, 2004, 2006; *Wildenschild et al.*, 2005] we imposed pressure boundary conditions instead because in numerical experiments we found that flux boundary conditions would lead to early breakthrough of wetting or nonwetting fluid. Wetting phase saturation was determined by calculating the fraction of the pore volume where the W component density, $n_2(\mathbf{x})$, was greater than the NW component density, $n_1(\mathbf{x})$.

[36] Three series of LB simulations were conducted: primary drainage, primary imbibition, and secondary drainage. Nine single step primary drainage points were simulated with final P_c at 91, 182, 272, 362, 453, 541, 631, 793, 980 Pa. Nine primary imbibition steps were simulated for final pressures at 980, 808, 631, 453, 362, 273, 182, 99 and 0 Pa. Finally, we carried out four secondary drainage simulations with final $P_c = 182, 362, 541, \text{ and } 631$ Pa. The simulated pressures are identified by symbols at the bottom of Figure 5. The P_c listed here are the final pressures

derived from the pressures at the W and NW boundaries and are not always exactly the same for drainage and imbibition. The small discrepancies are probably a result of accumulated numerical errors and a small degree of disequilibrium in the samples. All simulations were carried out with single pressure steps starting from a fully W phase saturated medium (primary drainage) or NW phase saturated medium (primary imbibition), with the exception of the secondary drainage simulations which were started from the final saturation field of the $P_c = 0$ Pa primary imbibition simulation. The objective of each simulation was to reach an equilibrium state where there was no more change in sample W phase saturation, S . In most cases we ran the simulations for $5 \cdot 10^5$ or more iterations, equal to at least 25 s of physical time for the water-air system. Except for the highest saturations it was not practically feasible to reach an absolute state of equilibrium within this time frame. We therefore also accepted some simulations that were in near-equilibrium as judged from saturation versus time graphs (for example, $P_c = 541$ and 631 Pa in Figure 6a, and $P_c = 362$ Pa in Figure 6b for primary imbibition). Although no strict guidelines were used to determine equilibrium, it turned out that all accepted simulations had absolute saturation changes ($|\Delta S|$) smaller $< 0.01 \text{ s}^{-1}$ for the last 20,000 iterations of the simulations (i.e., the last second of physical time).

4. Results and Discussion

[37] Time series of wetting phase saturations for the three simulations series appear in Figures 6a and 6b and show that hundreds of thousands of iterations were needed to reach (near) equilibrium. Although most simulations reached equilibrium, complete equilibrium was not reached for the 541 and 631 Pa pressures for the drainage simulations ($|\Delta S| = 0.0065$ and 0.0019 s^{-1} , respectively, for the last physical second of the simulations) and the 362 Pa simulation for imbibition ($|\Delta S| = 0.0034 \text{ s}^{-1}$). Each of these simulations was run for $5 \cdot 10^5$ iterations, a number that allowed equilibrium for lower pressures. However, the $P_c = 980$ Pa drainage simulation shows that one million iterations may be needed to reach a more complete equilibrium at the higher P_c values ($|\Delta S| = 1.2 \cdot 10^{-4} \text{ s}^{-1}$ for $P_c = 980$ Pa). The 0, 98 (not shown) and 182 Pa imbibition simulations appear to reach near-equilibrium between $0.5 \cdot 10^5$ and $1.5 \cdot 10^5$ iterations, after which the saturation keeps increasing slowly ($|\Delta S| = 9.4 \cdot 10^{-4} \text{ s}^{-1}$ for $P_c = 0$ Pa). As discussed later, these simulations have an entrapped NW phase bubble that slowly evaporates, thus causing a gradual increase in saturation. Despite these issues we are confident that the near-equilibrium results can be used for a comparison with the experimental data.

[38] Profiles of average wetting phase saturation for the $P_c = 980$ Pa drainage step is shown in Figure 7a. Likewise, Figure 7b shows data for the $P_c = 0$ Pa imbibition step. Dashed lines are plotted for every $1 \cdot 10^4$ iterations until $9 \cdot 10^4$ iterations and solid lines for every 10^5 iterations thereafter. Both simulations reached near-equilibrium, but the imbibition step did so in approximately $1 \cdot 10^5$ iterations, whereas the drainage step required many more iterations, most likely because of very low hydraulic conductivities once low saturations were reached. There is asymmetry in how the profiles saturate and drain over time.

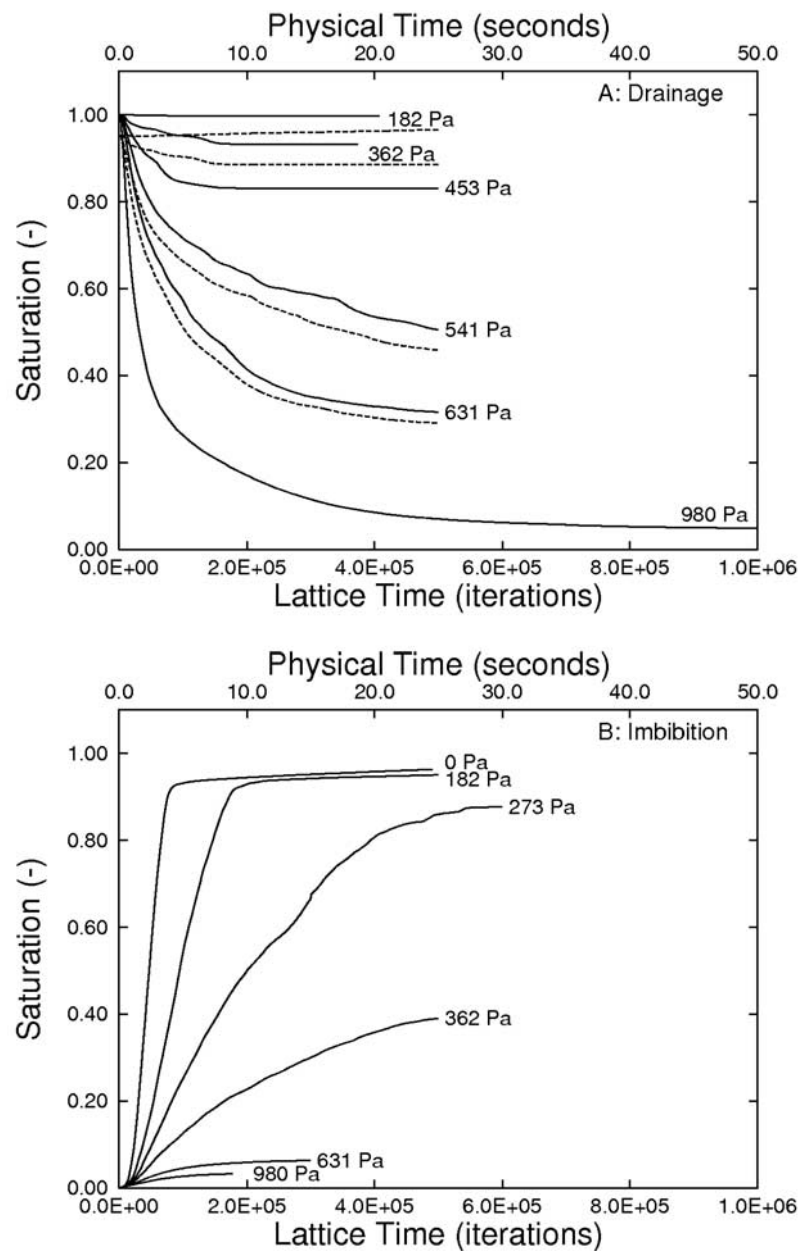


Figure 6. Evolution of the wetting phase saturation in lattice time (iterations) and physical time (seconds, valid for the water-air system) for selected (a) primary (solid lines) and secondary drainage (dashed lines) simulations and (b) primary imbibition simulations.

In the case of imbibition, there appears to be a wetting front migrating upward, followed by NW phase entrapment and migration of the NW phase bubble as indicated by the crossing of early time dashed lines and late time solid lines. In the drainage simulation there appears to be a rapid initial desaturation that decreases downward during the first $2 \cdot 10^4$ iterations after which the profile desaturates more uniformly with height. Physical time for these simulations (equation (13)) is on the order of 25 to 50 s for imbibition and drainage, respectively.

[39] Final saturation profiles of all simulations appear in Figures 7c and 7d for drainage and imbibition, respectively. Figure 7c shows that the NW phase does not percolate to the bottom of the sample for pressures of 91, 182, 272, 362, and

453 Pa, making it difficult to assign a representative saturation for these simulations. We note that similar saturation gradients were observed in this pressure range for the experimental data presented by *Culligan et al.* [2006]. The nonuniform saturation for these pressures indicates that NW phase entry is controlled by a percolation effect. To some extent, the percolation effect appears to exist also for the 541 and 631 Pa pressures. Although the NW phase does break through to the bottom for these pressures, the profiles also exhibit a gradual increase of saturation with depth. The 793 and 980 Pa drainage simulations, which were run for 10^6 instead of $5 \cdot 10^5$ iterations, show constant saturations indicating a more complete NW phase percolation. At these pressures the residual W phase is present as liquid bridges

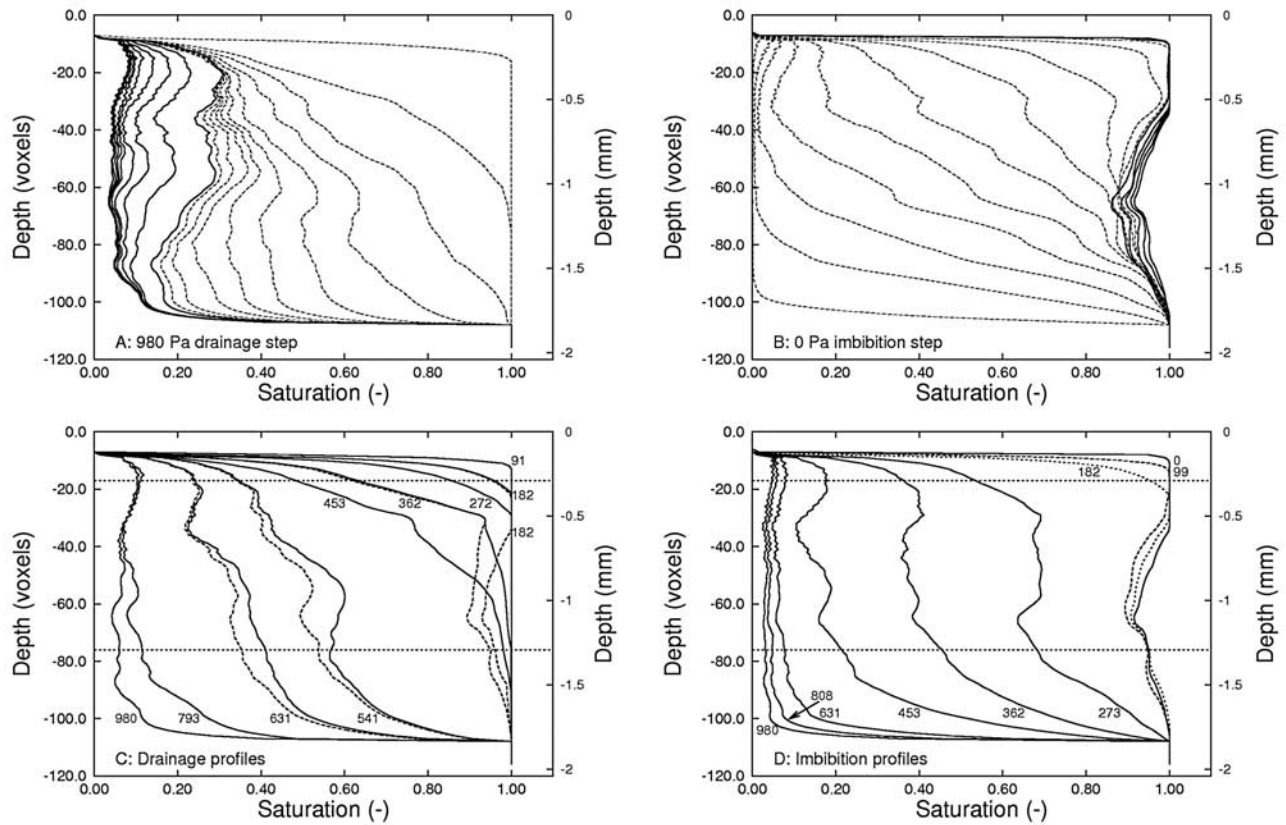


Figure 7. Simulated wetting phase saturation profiles. (a) Evolution of the saturation profile for 0 to 980 Pa primary drainage step and (b) an imbibition step to 0 Pa for a initially fully NW saturated medium. Dashed lines in Figures 7a and 7b are for every 10,000 iterations until 90,000 iterations; thereafter solid lines denote every 100,000 iterations. Final saturation profiles for the (c) drainage and (d) imbibition steps. Dashed lines in Figure 7c denote the secondary drainage steps. The area between the horizontal lines in Figures 7c and 7d indicate the section that was used to calculate saturations. Dashed lines were used in Figure 7d for 99 and 182 Pa to enhance legibility.

or situated in corners between glass beads, extensive liquid films were not present (results not shown). Secondary drainage profiles (Figure 7c, dashed line) have lower average saturations than their primary counterparts, and it is interesting to note that the 272 and 182 Pa secondary drainage simulations still show effects of the air entrapment that occurred during the preceding 0 Pa primary imbibition step. Figure 7d shows that, relative to the drainage simulations, the saturation profiles for imbibition are more uniform with depth. NW phase entrapment is clearly visible for 0, 99, and 182 Pa; the latter two curves have been plotted with dashed lines to improve readability.

[40] All simulations show strong saturation transitions near the discontinuities at the top ($z = -8$ voxels, non-wetting boundary) and the wetting filter at $z = -108$ voxels. The transition at the top can be explained by fluid interfaces that protrude from the nonwetting boundary but which have nonzero contact angles in smaller pores which therefore cannot be desaturated. Near the wetting filter, pore throats probably prevent the nonwetting phase to reach the larger pores above the wetting filter. Only when the NW phase entry point of the small pores is exceeded it is possible to further desaturate the pore space just above the filter. We note that these effects are pressure (and therefore curvature) dependent and extend over as much as half a millimeter. For

the present comparison it is important to exclude the saturation transitions near the boundaries. From Figure 7d it appears that the imbibition profiles yield approximately homogeneous saturations between $z = -16$ and -77 voxels, allowing a reasonable average saturation to be computed. This is, unfortunately, not the case for the drainage profiles in Figure 7c where no homogeneous conditions appear to exist between $P_c = 99$ and 631 Pa. Averages of these profiles should therefore be used with caution.

[41] Measured pressure-saturation graphs from *Culligan et al.* [2004, 2006] along with simulated results for the water-air and water-Soltrol systems appear in Figures 8a and 8b, respectively. The simulated results in these graphs are identical, and differ only in the capillary pressures that were calculated using equation (12) and the applicable surface tension.

[42] The water-air graph shows an encouraging correspondence between the observations and the simulations. Imbibition points match the observed data well and it is interesting to note that the simulated air entrapment at $P_c = 0, 99,$ and 182 Pa (saturation is 0.95) is close to measured data at similar pressures. Simulated drainage points seem to transition from the measured primary drainage curve at $P_c = 91, 182$ and 272 Pa to the measured secondary drainage characteristic ($P_c = 372$ Pa and higher pressures). It appears

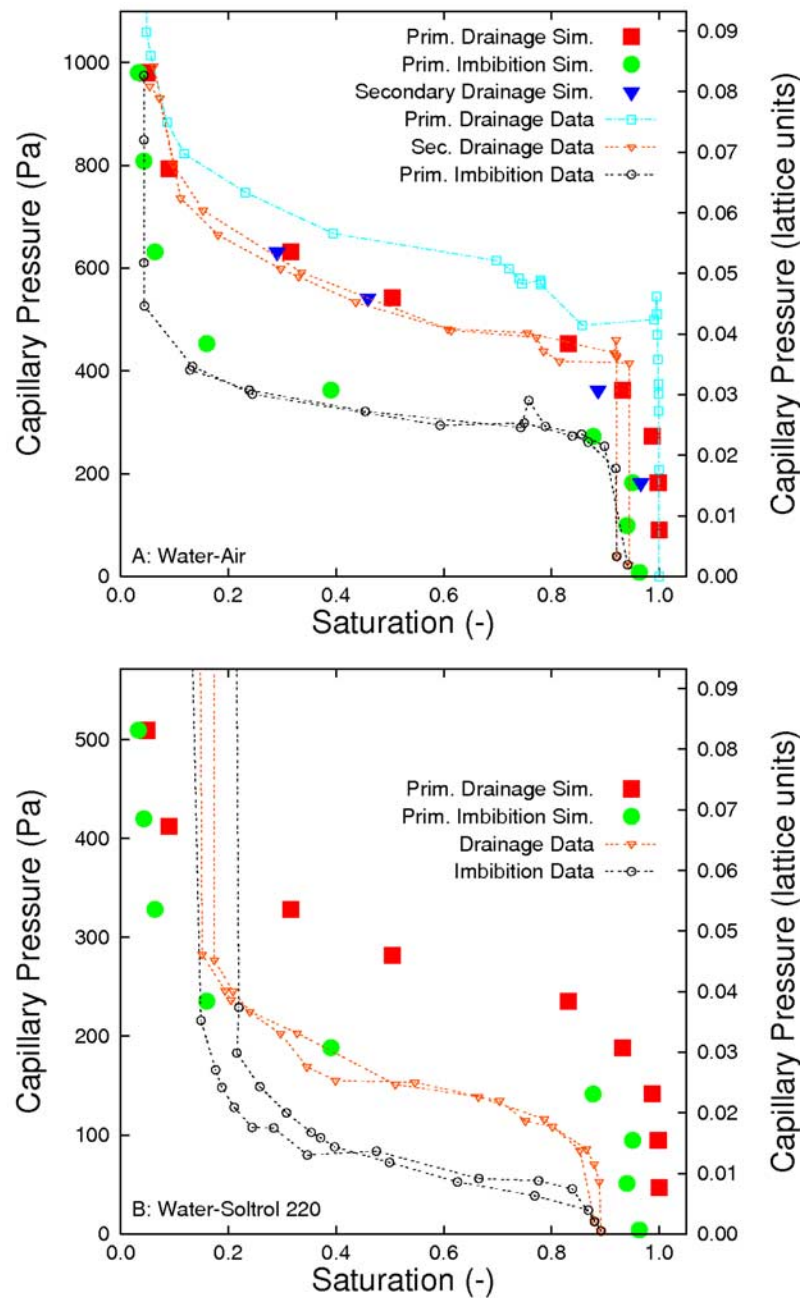


Figure 8. Simulated (large symbols) and measured (small symbols connected with lines) pressure-saturation characteristics for the (a) water-air and (b) water-Soltrol systems. Data points for secondary drainage simulations were deleted from Figure 8b for clarity.

that the nonwetting phase entry point of the primary drainage simulations is somewhat lower than that of the experimental primary drainage curve. However, referring to the inhomogeneous drainage saturation profiles between $P_c = 91$ and 632 Pa (Figure 7c) it is difficult to make an objective comparison. The saturations of the simulated secondary drainage points are situated just below the simulated primary points and are in good agreement with the measured data.

[43] Results for the water-Soltrol system are less convincing, with simulated saturations generally higher than experimental data for saturations greater than 0.2. Culligan

et al. [2006] already reported some problems with these measurements and attributed the high residual water saturations and high Soltrol entrapment near $P_c = 0$ Pa to gaps between the wall of the column and the sintered glass bead mass. Inspection of the experimental data further shows that the experimental water-air and water-Soltrol data cannot be normalized to one graph by dividing the measured capillary pressure with the surface tension (results not shown). From this analysis it appears that the water-Soltrol system has a surface tension that is much lower than reported in the literature [Bradford and Leij, 1996; Kechavarzi *et al.*, 2000, 2005; Liu *et al.*, 1998; Schroth *et al.*, 1995]. In fact, a

reasonable agreement between simulated results and experimental data is found at the wet end of the graph if the surface tension in equation (12) is set to an unrealistically low value of 0.018 N/m (results not shown). A more plausible explanation is that the contact angle of the water-Soltrol-glass system is not zero, which would not only lower the capillary pressure, but also cause a different fluid structure inside the porous medium (and thus require another series of LB simulations). We are currently performing additional experiments and simulations to understand the water-Soltrol system.

5. Summary and Conclusion

[44] In this study we have applied a multiphase lattice Boltzmann model [Martys and Chen, 1996] to microtomographic data [Culligan et al., 2004, 2006] and found an encouraging agreement between observed and simulated water-air pressure-saturation characteristics. Results for a water-Soltrol system were somewhat disappointing, however. Several steps and assumptions were needed.

[45] First of all, it was necessary to demonstrate that gravitational, inertial, and viscous forces were negligible compared to the capillary forces inside the experimental system, making it possible to simulate both systems with the Shan-Chen model. Secondly, a numerical calibration using 2-D and 3-D simulations was needed to achieve a reasonable lattice surface tension and a prescribed contact angle of zero. Results from these simulations also provided us with a means to set the pressure boundary conditions for our LB simulations, allowing us to control the capillary pressure inside the sample. By using pressure scaling from the lattice space to the experimental conditions we were able to assign physical capillary pressures to LB results that were applicable to water-air and water-Soltrol systems, a finding that has not been presented previously. Only one simulation was needed to represent a pressure point in each of these systems. Time scaling indicated that about 10^6 iterations are needed to simulate 50 s in a water-air system.

[46] Primary drainage (nine points), primary imbibition (nine points), and secondary imbibition (four points) were simulated. A good match was found between simulated and imaged pressure-saturation data for the water-air system, but the results for the water-Soltrol system were not as satisfying. The simulated water-Soltrol results appeared to have higher NW phase entry pressures than the experimental data and were unable to deal with the high residual wetting-phase saturations that were found in the experiments. As reported by Culligan et al. [2006] there appear to be some problems with the present water-Soltrol data and additional work is under way to collect a better data set (CMT data available at http://cbee.oregonstate.edu/research/multiphase_data/).

[47] An interesting finding was that we were able to simulate nonwetting phase entrapment during imbibition that was similar to measured values for the air-water system. We also found that there are saturation transitions in the porous medium near the wetting and nonwetting boundaries. This effect appears to be pressure (and therefore curvature) dependent and is probably caused by the presence of pore necks and percolation effects.

[48] Typical simulations for each pressure point lasted about four weeks on a system with four CPUs. Faster simulations were possible by using more CPUs [cf. Pan et al., 2004b], but on the computer clusters we used for this study, we found that the greatest number of simulations could be done when each job was limited to four CPUs. The present LB simulations are currently much slower than pore-network models which are able to yield similar results [e.g., Vogel et al., 2005]. However, for a pore-network model it is necessary to transform complex pore geometry into simple elementary pores, whereas for a LB model the observed pore geometry can be used directly in the simulations while simulated fluid geometry can also be directly compared to observations. In addition, it is likely that continuous improvements in computer hardware and software methods will lead to much faster LB simulations in the future.

[49] The present study focused mainly on obtaining a proper physical representation of the experimental conditions with the S-C lattice Boltzmann model and the simulation of pressure-saturation curves. Currently, we are working to extend the comparison between experimental data and numerical results to interfacial areas and curvatures, extract wetted solid fraction and contact line information and compare measured and simulated spatial distributions of wetting and nonwetting fluids. Such results will yield further insight into whether LB models can accurately simulate fluid phenomena at the pore scale and can be used to make extrapolations to the sample scale. Further simulations and LB model improvements [e.g., Inamuro et al., 2004a, 2004b; Li et al., 2005; Pan et al., 2006] may provide faster or more precise results and allow us to deal with rate-dependent pressure-saturation characteristics [e.g., Wildenschild et al., 2001]. With improved models it may also be possible to simulate large density and viscosity differences and test thermodynamic pressure-saturation-interfacial area theories as forwarded by Hassanizadeh and Gray [1993] and Gray et al. [2002].

[50] **Acknowledgments.** We thank the High Performance Computing systems at the Technical University of Denmark and the Colleges of Science and Engineering at Oregon State University for CPU time. We also thank the GeoSoilEnviro Consortium for Advanced Radiation sources (GSECARS) bending magnet beamline, Sector 13, Advanced Photon Source, Argonne National Laboratory. GeoSoilEnviroCARS is supported by the National Science Foundation—Earth Sciences (EAR-0217473), Department of Energy—Geosciences (DE-FG02-94ER14466), and the State of Illinois. Use of the APS was supported by the U.S. Department of Energy, Basic Energy Sciences, Office of Energy Research, under contract W-31-109-Eng-38. We are grateful to Willem Bouten and Petri de Willigen at the University of Amsterdam and Karsten Høgh-Jensen at the University of Copenhagen for discussions. Christensen and Wildenschild were supported, in part, by Statens Teknisk Videnskabelige Forskningsråd (STVF) in Denmark. Wildenschild and Porter were supported, in part, by NSF-EAR-0337711 and NSF-EAR-0610108. Schaap was supported, in part, by NSF-EAR-0337378, NSF-EAR-061003, NWO-ALW in the Netherlands, and USDA-ARS Salinity Laboratory, Riverside, California. Finally, we would like to thank the Associate Editor and the anonymous reviewers for their comments which have resulted in a substantially improved manuscript.

References

- Adler, P. M., C. G. Jacquin, and J. A. Quiblier (1990), Flow in simulated porous media, *Int. Multiphase Flow, J.*, 16(4), 691–712.
- Angelopoulos, A. D., V. N. Paunov, V. N. Burganos, and A. C. Payatakes (1998), Lattice Boltzmann simulation of nonideal vapor-liquid flow in porous media, *Phys. Rev. E*, 57, 3237–3245.

- Blair, S. C., P. A. Berge, and J. G. Berryman (1996), Using two-point correlation functions to characterize micro-geometry and estimate permeabilities of sandstones and porous glass, *J. Geophys. Res.*, *101*(B9), 20,359–20,375.
- Bradford, S. A., and F. J. Leij (1996), Predicting two- and three-fluid capillary pressure-saturation relationships of porous media with fractional wettability, *Water Resour. Res.*, *32*(2), 251–259.
- Chau, J. F., D. Or, and M. C. Sukop (2005), Simulation of gaseous diffusion in partially saturated porous media under variable gravity with lattice Boltzmann methods, *Water Resour. Res.*, *41*, W08410, doi:10.1029/2004WR003821.
- Chen, S., and G. D. Doolen (1998), Lattice Boltzmann method for fluid flows, *Annu. Rev. Fluid Mech.*, *30*, 329–364.
- Coles, M. E., R. D. Hazlett, E. L. Muegge, K. W. Jones, B. Andrews, B. Dowd, P. Siddons, A. Peskin, P. Spanne, and W. E. Soll (1998), Developments in synchrotron X-ray microtomography with applications to flow in porous media, *SPE Reservoir Eng. Eval. Eng.*, *1*(4), 288–296.
- Culligan, K. A., D. Wildenschild, B. S. B. Christensen, W. G. Gray, M. L. Rivers, and A. F. B. Tompson (2004), Interfacial area measurements for unsaturated flow through a porous medium, *Water Resour. Res.*, *40*, W12413, doi:10.1029/2004WR003278.
- Culligan, K. A., D. Wildenschild, B. S. B. Christensen, W. G. Gray, and M. L. Rivers (2006), Pore-scale characteristics of multiphase flow in porous media: a synchrotron-based CMT comparison of air-water and oil-water experiments, *Adv. Water Resour.*, *29*, 227–238.
- Ferréol, B., and D. H. Rothman (1995), Lattice Boltzmann simulations of flow through Fontainebleau sandstone, *Transp. Porous Media*, *20*, 3–20.
- Gray, W. G., A. F. B. Tompson, and W. E. Soll (2002), Closure conditions for two-fluid flow in porous media, *Transp. Porous Media*, *47*, 29–65.
- Gunstensen, A. K., and D. H. Rothman (1991), Lattice Boltzmann model for immiscible fluids, *Phys. Rev. A*, *43*, 4320–4327.
- Hassanzadeh, S. M., and W. G. Gray (1993), Thermodynamic basis of capillary pressure in porous media, *Water Resour. Res.*, *29*(20), 3389–3405.
- Házi, G., A. T. Imre, G. Mayer, and I. Farkas (2002), Lattice Boltzmann methods for two-phase flow modeling, *Ann. Nuclear Energy*, *29*, 1421–1453.
- Hazlett, R. D. (1995), Simulation of capillary dominated displacements in microtomographic images of reservoir rocks, *Transp. Porous Media*, *20*, 21–35.
- Heijs, A. W. J., and C. P. Lowe (1995), Numerical evaluation of the permeability and the Kozeny constant for two types of porous media, *Phys. Rev. E*, *61*, 4346–4352.
- Hilpert, M., and C. T. Miller (2001), Pore-morphology-based simulations of drainage in totally wetting porous media, *Adv. Water Resour.*, *24*, 243–255.
- Hilpert, M., J. F. McBride, and C. T. Miller (2001), Investigation of the residual funicular nonwetting-phase-saturation relation, *Adv. Water Resour.*, *24*, 157–177.
- Inamuro, T., T. Ogata, S. Tajima, and N. Konishi (2004a), A lattice Boltzmann method for incompressible two-phase flows with large density differences, *J. Comput. Phys.*, *198*, 628–644.
- Inamuro, T., T. Ogata, and F. Ogino (2004b), Numerical simulation of bubble flow by the lattice Boltzmann method, *Future Generation Comput. Syst.*, *20*, 959–964.
- Kechavarzi, C., K. Soga, and P. Wiart (2000), Multispectral image analysis method to determine dynamic fluid saturation distribution in two-dimensional three-fluid phase flow laboratory experiments, *J. Contam. Hydrol.*, *46*, 265–293.
- Kechavarzi, C., K. Soga, and T. H. Illangasekare (2005), Two-dimensional laboratory simulation of LNAPL infiltration and redistribution in the vadose zone, *J. Contam. Hydrol.*, *76*, 211–233.
- Li, H., C. Pan, and C. T. Miller (2005), Pore-scale investigation of viscous coupling effects for two-phase flow in porous media, *Phys. Rev. E*, *72*, 026705.
- Liu, Y. P., J. W. Hopmans, M. E. Grismer, and J. Y. Chen (1998), Direct estimation of air-oil and oil-water capillary pressure and permeability relations from multi-step outflow experiments, *J. Contam. Hydrol.*, *32*, 223–245.
- Martys, N. S., and H. Chen (1996), Simulation of multicomponent fluids in complex three-dimensional geometries by the lattice Boltzmann method, *Phys. Rev. E*, *53*, 743–750.
- Martys, N. S., and J. F. Douglas (2001), Critical properties and phase separation in lattice Boltzmann fluid mixtures, *Phys. Rev. E*, *63*, 031205.
- Masad, E., B. Muhunthan, and N. Martys (2000), Simulation of fluid flow and permeability in cohesionless soils, *Water Resour. Res.*, *36*(4), 851–864.
- Nordhaug, H. F., M. Celia, and H. K. Dahle (2003), Pore network model for calculation of interfacial velocities, *Adv. Water Resour.*, *26*, 1061–1074.
- Nourgaliev, R. R., T. N. Dinh, T. G. Theofanous, and D. Joseph (2003), The lattice Boltzmann equation method: Theoretical interpretation, numerics and implications, *Int. Multiphase Flow. J.*, *29*, 117–169.
- Pan, C., M. Hilpert, and C. T. Miller (2001), Pore-scale modeling of saturated permeabilities in random sphere packings, *Phys. Rev. E*, *64*, 6702.
- Pan, C., M. Hilpert, and C. T. Miller (2004a), Lattice-Boltzmann simulation of two-phase flow in porous media, *Water Resour. Res.*, *40*, W01501, doi:10.1029/2003WR002120.
- Pan, C., J. F. Prins, and C. T. Miller (2004b), A high-performance lattice Boltzmann implementation to model flow in porous media, *Comput. Phys. Commun.*, *158*, 89–105.
- Pan, C., L.-S. Luo, and C. T. Miller (2006), An evaluation of lattice Boltzmann schemes for porous medium flow simulation, *Comput. Fluids*, *35*(2), 898–909.
- Prodanović, M., W. B. Lindquist, and R. S. Seright (2006), Porous structure and fluid partitioning in polyethylene cores from 3D X-ray microtomographic imaging, *J. Colloid Interface. Sci.*, *298*, 282–297.
- Qian, Y. H., P. Lallemand, and D. d’Humières (1992), Lattice BGK models for Navier-Stokes equation, *Europhys. Lett.*, *17*, 479–484.
- Raiskinmäki, P., A. Shakib-Manesh, A. Jäsberg, A. Koponen, J. Merikoski, and J. Timonen (2001), Lattice-Boltzmann simulation of capillary rise dynamics, *J. Stat. Phys.*, *107*, 143–158.
- Rothman, D. H., and J. M. Keller (1988), Immiscible cellular automaton fluids, *J. Stat. Phys.*, *52*, 1119–1127.
- Schaap, M. G., and I. Lebron (2001), Using microscope observations of thin sections to estimate soil permeability with the Kozeny-Carman Equation, *J. Hydrol.*, *251*, 186–201.
- Schroth, M. H., J. D. Istok, S. J. Ahearn, and J. S. Selker (1995), Geometry and position of light nonaqueous-phase liquid lenses in water-wetted porous media, *J. Contam. Hydrol.*, *19*, 269–287.
- Shan, X., and H. Chen (1993), Lattice Boltzmann model for simulating flows with multiple phases and components, *Phys. Rev. E*, *47*, 1815–1819.
- Shan, X., and H. Chen (1994), Simulations of non ideal gases and liquids-gas phase transitions by the lattice Boltzmann equation, *Phys. Rev. E*, *49*, 2941–2948.
- Shan, X., and G. Doolen (1996), Diffusion in a multicomponent lattice Boltzmann model, *Phys. Rev. E*, *54*, 3614–3620.
- Succi, S. (2001), *The Lattice Boltzmann Equation for Fluid Flow and Beyond*, Oxford Sci., Oxford, U.K.
- Sukop, M. C., and D. Or (2004), Lattice Boltzmann method for modeling liquid-vapor interface configurations in porous media, *Water Resour. Res.*, *40*, W01509, doi:10.1029/2003WR002333.
- Swift, M. R., W. R. Osborn, and J. M. Yeomans (1995), Lattice Boltzmann simulation of nonideal fluids, *Phys. Rev. Lett.*, *75*, 830–833.
- Swift, M. R., E. Orlandini, W. R. Osborn, and J. M. Yeomans (1996), Lattice Boltzmann simulations of liquid-gas and binary fluid systems, *Phys. Rev. E*, *54*, 5041–5052.
- Tölke, J., M. Krafczyk, M. Schultz, and E. Rank (2002), Lattice Boltzmann simulations of binary fluid flow through porous media, *Philos. Trans. R. Soc., Ser. A*, *360*, 535–545.
- Vogel, H.-J. (2000), A numerical experiment on pore size, pore connectivity, water retention, permeability, and solute transport using network models, *Eur. J. Soil. Sci.*, *51*, 99–105.
- Vogel, H.-J., J. Tölke, V. P. Schultz, M. Krafczyk, and K. Roth (2005), Comparison of a lattice-Boltzmann model, full morphology model, and a pore network model for determining capillary pressure-saturation relationships, *Vadose Zone J.*, *4*, 380–388.
- Wildenschild, D., J. W. Hopmans, and J. Simunek (2001), Flow rate dependence of soil hydraulic properties, *Soil Sci. Soc. Am. J.*, *65*(1), 35–48.
- Wildenschild, D., J. W. Hopmans, C. M. P. Vaz, M. L. Rivers, D. Rikard, and B. S. B. Christensen (2002), Using X-ray computed tomography in hydrology: Systems, resolutions, and limitations, *J. Hydrol.*, *267*, 285–297.
- Wildenschild, D., J. W. Hopmans, M. L. Rivers, and A. J. R. Kent (2005), Quantitative analysis of flow processes in a sand using synchrotron-based X-ray microtomography, *Vadose Zone J.*, *4*, 112–126.
- Zhang, D., R. Zhang, S. Chen, and W. E. Soll (2000), Pore scale study of flow in porous media: Scale dependency, REV, and statistical REV, *Geophys. Res. Lett.*, *27*, 1195–1198.
- Zhang, X., A. G. Bengough, and L. K. Deeks (2002a), A novel three-dimensional lattice Boltzmann model for solute transport in variably saturated soils, *Water Resour. Res.*, *38*(9), 1167, doi:10.1029/2001WR000982.

Zhang, X., A. G. Bengough, J. W. Crawford, and I. M. Young (2002b), A lattice BGK model for advection and anisotropic dispersion equation, *Adv. Water Resour.*, 25, 1–8.

Zhang, X., L. K. Deeks, A. G. Bengough, J. W. Crawford, and I. M. Young (2005), Determination of the soil hydraulic conductivity with the lattice Boltzmann method and soil thin-section technique, *J. Hydrol.*, 306, 59–70.

M. L. Porter and D. Wildenschild, Department of Chemical, Biological, and Environmental Engineering, Oregon State University, Corvallis, OR 97331, USA.

M. G. Schaap, Department of Soil, Water and Environmental Science, Shantz Building, University of Arizona, Tucson 85721, USA. (mschaap@cals.arizona.edu)

B. S. B. Christensen, Department of Hydrology, Geological Survey of Denmark and Greenland (GEUS), Øster Voldgade 10, DK-1350 Copenhagen, Denmark.